Journal of Southeast University (English Edition) Vol. 26, No. 3, pp. 436 – 443 Sept. 2010 ISSN 1003—7985

Wind tunnel test for wind pressure characteristics on a saddle roof

Dong Xin Ye Jihong

(Key Laboratory of Concrete and Pre-Stressed Concrete Structures of Ministry of Education, Southeast University, Nanjing 210096, China)

Abstract: The wind pressure characteristics on a saddle roof at wind direction along the connection of the low points are systematically studied by the wind tunnel test. First, the distributions of the mean and the fluctuating pressures on the saddle roof are provided. Through the wind pressure spectra, the process of generation, growth and break down of the vortex on the leading edge is presented from a microscopic aspect and then the distribution mechanism of the mean and fluctuating pressures along the vulnerable leading edge is explained. By analysis of the wind pressure spectra near the high points, it can be inferred that the body induced turbulence reflects itself as a high-frequency pressure fluctuation. Secondly, the third- and fourth-order statistical moments of the wind pressure are employed to identify the non-Gaussian nature of the pressure time history and to construct an easy tool to localize regions with a non-Gaussian feature. The cause of the non-Gaussian feature is discussed by virtue of the wind pressure spectra. It is concluded that the non-Gaussian feature of the wind pressure originates from the effects of flow separation and body-induced turbulence, and the former effect plays an obvious role.

Key words: saddle roof; mechanism of wind pressure distribution; wind pressure spectra; non-Gaussian feature

A long-span roof, which possesses a large span height ratio, is usually located at the bottom of the atmospheric boundary layer. As a result of the particular structural shape and high turbulence intensity of the atmospheric boundary layer, wind pressures on the roof surface exhibit complex fluctuating characteristics. The wall pressure fluctuations at one location are the result of the integral effects of the large-scale low-frequency structure in the far-field region and the small-scale high-frequency structure in the near-field region[1]. Therefore, it is necessary to consider the incident wind turbulence as well as the body induced turbulence (BIT) in order to understand the mechanism of pressure fluctuating characteristics. Pressure spectra, due to their high resolution in the frequency domain, are often utilized to identify potential sources of turbulence. Kasperski et al. [2] presented four spectral shapes for upwind, separation, reattachment and downwind, respectively, but no specific formula. Chen[1] analyzed power spectra of pressure fluctuation for different sites on a gable roof and located regions with the same spectral pattern. Suresh Kumar et al. [3] suggested that the exponential function can be employed to represent normalized spectra for various zones of low building roofs. In addition to the complicated characteristics of pressure fluctuation, Stathopoulos et al. [4–5] pointed out that the probability density function (PDF) of wind pressure for corner zones and separated flow regions shows a departure from the standard normal distribution. Through statistical moments of the third and the fourth order, zones of the Gaussian and non-Gaussian pressure fluctuations were presented for low-rise buildings[6] and large-span flat roofs[7]. Gioffre et al. [8] utilized histograms of experimental data to localize regions with a non-Gaussian feature on prismatic tall buildings. Ko et al. [9] pointed out that non-Gaussian local wind pressures have a much higher probability for the larger negative pressure than those indicated by the Gaussian assumption. Hou[10] showed that zones of the Gaussian and non-Gaussian pressure fluctuations for large-span roofs obtained from higher-order statistical moments of pressure fluctuations are nearly consistent with that from the curve fitting method based on the k-s test.

So far researches on the non-Gaussian feature are concentrated on description, localization and numerical simulation. The in-depth explanation on the mechanism of non-Gaussian features is not available. To address the above issue, wind pressure characteristics on a saddle roof are investigated through the wind tunnel test. First, the pressure distributions are presented under specific wind directions. Based on the vortex movement, the mechanism of wind pressure variations along the vulnerable leading edge is clarified. Next, the zones of the Gaussian and non-Gaussian pressure fluctuations are determined, and the mechanisms of non-Gaussian features are interpreted.

1 Wind Tunnel Experiment of Saddle Roof

1.1 Facilities and instrumentation

The pressure measurement experiments are carried out in the HD-2 atmospheric boundary layer wind tunnel at the Wind Engineering Research Center of Hunan University, Changsha, China. The tests are conducted in the high-speed working section which is 17 m long, 3 m wide and 2.5 m high. The reference wind velocities are measured by the hot-wire anemometer. Pressure data are obtained using a PSI electronic pressure scanning system, as well as the INV306 and DASP data acquisition and analysis system.

1.2 Model design

The model of a saddle roof (see Fig. 1) is manufactured using Plexiglas in order to obtain a "rigid" body. It has a 100 mm height rise and a square platform with a diagonal equal to 600 mm. The rise-span ratio is 1/6. The heights of the low and high points are 0 and 200 mm, respectively.

Based on the blockage requirement and the size of the working section, a length ratio of 1∶200 is chosen. Beyond geometric similarity, the Strouhal number *St* for the scaled

Received 2009-09-18.

Biographies: Dong Xin (1982—), female, graduate; Ye Jihong (corresponding author), female, doctor, professor, yejihong@seu.edu.cn.

Foundation items: The National Natural Science Foundation of China (No. 50678036), Jiangsu Civil Engineering Graduate Center for Innovation and Academic Communication Foundation.

Citation: Dong Xin, Ye Jihong. Wind tunnel test for wind pressure characteristics on a saddle roof[J]. Journal of Southeast University (English Edition), 2010, 26(3): 436 – 443.

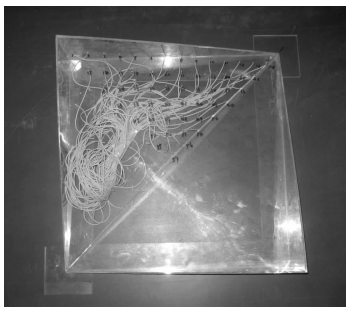

Fig. 1 Model of saddle roof

model is kept in accordance with that for the actual structure in this unsteady wind tunnel test. That is

$$\frac{f_m D_m}{U_m} = \frac{f_p D_p}{U_p} \tag{1}$$

where f is the frequency, D is the geometrical dimension, and U is the wind velocity. The subscripts m and p denote the model and the prototype, respectively. The ratio of wind speed and duration is set to 1∶2 and 1∶100, respectively. The scaling laws used in this test are reported in Tab. 1.

Tab. 1 Scaling laws for the wind tunnel test

Parameters	Model	Full-scale
Dimension/mm	600	120 000
Velocity/(m·s^{-1})	10	20
Time/s	20.3	2 030

In this wind tunnel test, the model is placed on the center of a wooden turntable, which is rotated to simulate different wind directions. Fig. 2 shows the locations of the taps and the angles of incidence.

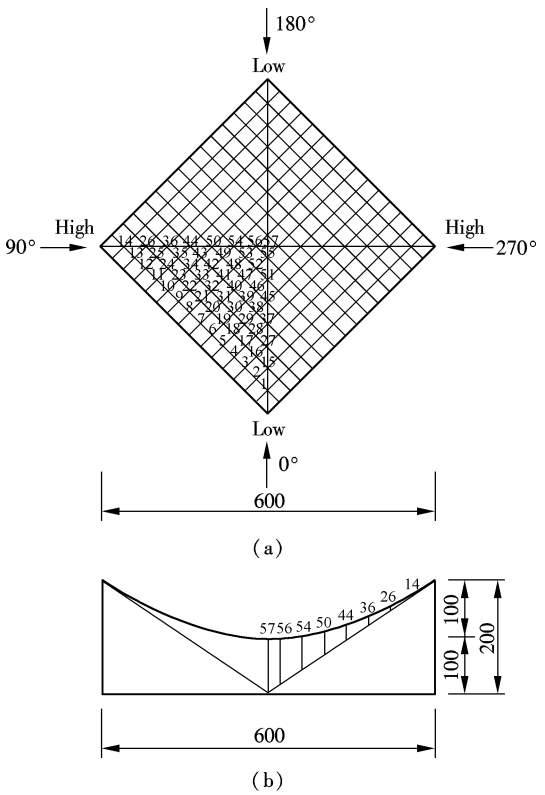

Fig. 2 Tap locations and definition of flow direction. (a) Top view; (b) Side view(unit: mm)

1.3 Simulation of atmospheric boundary layer

The terrain condition of category B (Power law exponent for mean velocity profile $\alpha = 0.16$) is created by placing roughness elements in the entrance portion of the test section. Fig. 3 shows the experimental profiles of mean speed and turbulence intensity, and the longitudinal spectra of incident wind.

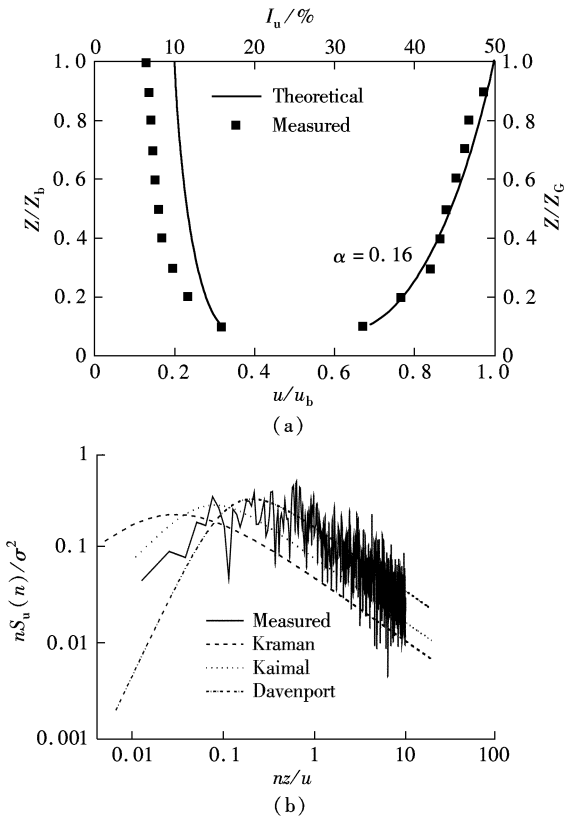

Fig. 3 Wind tunnel simulation for terrain B. (a) Mean velocity and turbulent intensity profile; (b) Longitudinal spectra of incident flow

The cutoff frequency is 1.5 Hz. The Kaimal spectrum indicates that the energy is very small at this frequency. Based on Eq. (1), we can obtain $f_m = f_p\left(\frac{U_m}{U_p}\right)\left(\frac{D_p}{D_m}\right)$. As previously mentioned, the length and velocity scales are 1∶200 and 1∶2, respectively. Thus $f_m = 150$ Hz. Based on the Nyquist theorem, the sampling rate must be at least $2f_m$, or else some high-frequency components in the input signal will not be correctly represented in the digitized output[11]. Therefore, the experimental sampling frequency should not be less than 300 Hz. In this test, pressure data are measured at a sampling rate of 325 Hz, meeting the above requirement. The sampling time is 20.3 s, resulting in a sample block of 6 600 values for each tap.

1.4 Data processing

The measured pressure data are converted to pressure coefficients by dividing them by the reference dynamic pressure at a height of 40 cm.

$$C_{p,i}(t) = \frac{P_i(t) - P_\infty}{\frac{1}{2}\rho V_h^2} \quad (2)$$

where $P_i(t)$ is the total pressure; P_∞ is the static pressure at 40 cm; ρ is the mass density of air; and V_h is the mean wind velocity at 40 cm. The mean wind pressure coefficient $C_{p,i,mean}$ and the fluctuating (root mean square) wind pressure coefficient $C_{p,i,rms}$ can be estimated by

$$C_{p,i,mean} = \frac{1}{N}\sum_{j=1}^{N} C_{p,ij} \quad (3)$$

$$C_{p,i,rms} = \sqrt{\sum_{j=1}^{N} \frac{C_{p,ij} - C_{p,i,mean})^2}{N-1}} \quad (4)$$

where the number of data points $N = 6\,600$.

The sign of pressure is specified as follows: Downward or inward pressure is positive, and upward or outward pressure (suction) is negative.

2 Results and Discussion

The pressure measurements are made for wind direction (see Fig. 2) varied from 0° to 345° in 15° steps, with a focus on the characteristics of wind pressure distribution in the case of 0°.

2.1 Mean and fluctuating pressure distribution

Fig. 4 shows contour maps of mean and root mean square (rms) pressure coefficients, respectively. The hatched zones in Fig. 4(a) indicate that the mean pressure coefficient is smaller than −0.8; or, in other words, that the mean suction is larger than 0.8. The gray zones in Fig. 4(b) denote that the rms pressure coefficient is larger than 0.2.

As shown in Fig. 4(a), the signs of roof surface pressure are observed to be negative for all the locations other than individual taps located near the windward corner. Local severe suctions are formed in the vicinity of high points, but the largest suction is not located at the high points. Besides, intense suctions also occur at the central concavity where the approaching flow separates.

Larger rms pressures are found at the middle of the leading edge, as illustrated in Fig. 4(b). The greatest suction fluctuation is located near the high points, while rms values in other regions remain roughly equivalent.

2.2 Characteristics of wind pressure spectra along the leading edge

In virtue of the vulnerability of the leading edge that sustains intense mean and fluctuating suction, the spectra of pressure fluctuation and vortex movement over this region are discussed in detail. The spectra of pressure fluctuation for tap 1 to tap 14 along the leading edge (see Fig. 2) are shown in Fig. 5. The spectra are normalized ($fS(f)/\sigma^2$) which is shown as a function of the reduced frequency, $F = fH/V$, where f is the frequency, H is a typical building dimension (The mean height of the structure is chosen for this study), V is the mean velocity at mean roof height, and σ is the standard deviation of fluctuating pressure. The reduced frequencies less than 0.1 are defined as low frequencies, those falling between 0.1 and 1 are middle frequencies, and those greater than 1 are called high frequencies. The mean and rms pressures of taps along the leading edge are shown in Tab. 2.

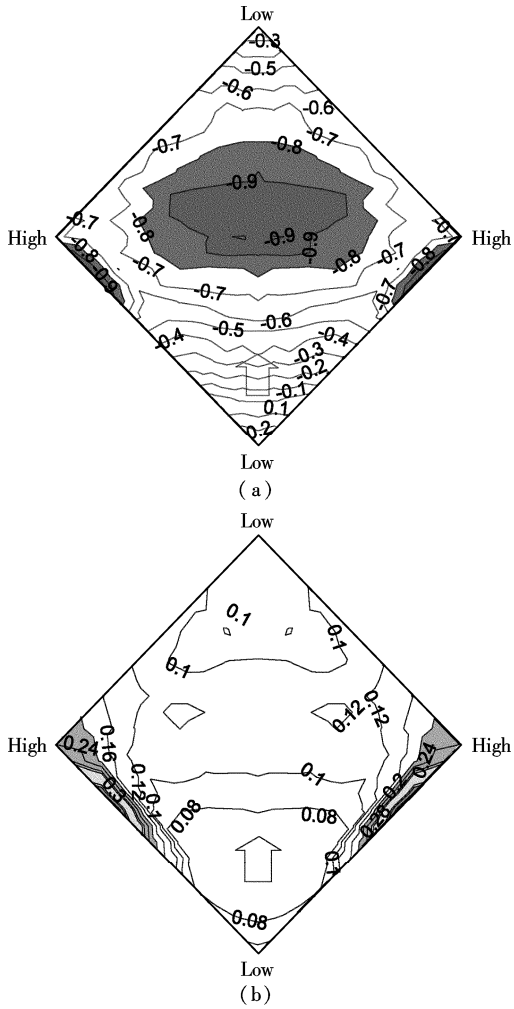

Fig. 4 Contour maps of mean and fluctuating pressure coefficients. (a) Mean pressure; (b) Fluctuating pressure

Tab. 2 Mean and fluctuating pressure of taps along leading edge

Tap	$C_{p,mean}$	$C_{p,rms}$	Tap	$C_{p,mean}$	$C_{p,rms}$
1	0.314 5	0.108 5	8	−0.484 6	0.246 2
2	0.231 5	0.097 9	9	−0.621 9	0.389 5
3	0.090 9	0.087 9	10	−0.868 4	0.491 8
4	0.036 1	0.082 4	11	−1.000 1	0.473 1
5	−0.143 0	0.079 8	12	−1.005 7	0.368 9
6	−0.232 7	0.106 4	13	−0.935 4	0.283 1
7	−0.360 5	0.163 7	14	−0.720 7	0.241 8

Fig. 5(a) displays pressure fluctuation spectra for taps 1 to 4 which are exposed to pressure. The spectra show a clear hump in the low-frequency range. The pressure fluctuations at these points can be postulated to be induced mainly by the turbulent content of the incident wind. The spectral energy of the humps and the rms pressure coefficients decrease with the increase in distance from the apex. This is called an upwind stage.

Fig. 5(b) gives wind pressure spectra for taps 5 to 7, from which suction begins to show. Energy in the low-frequency range decreases, whereas the energy in the middle-

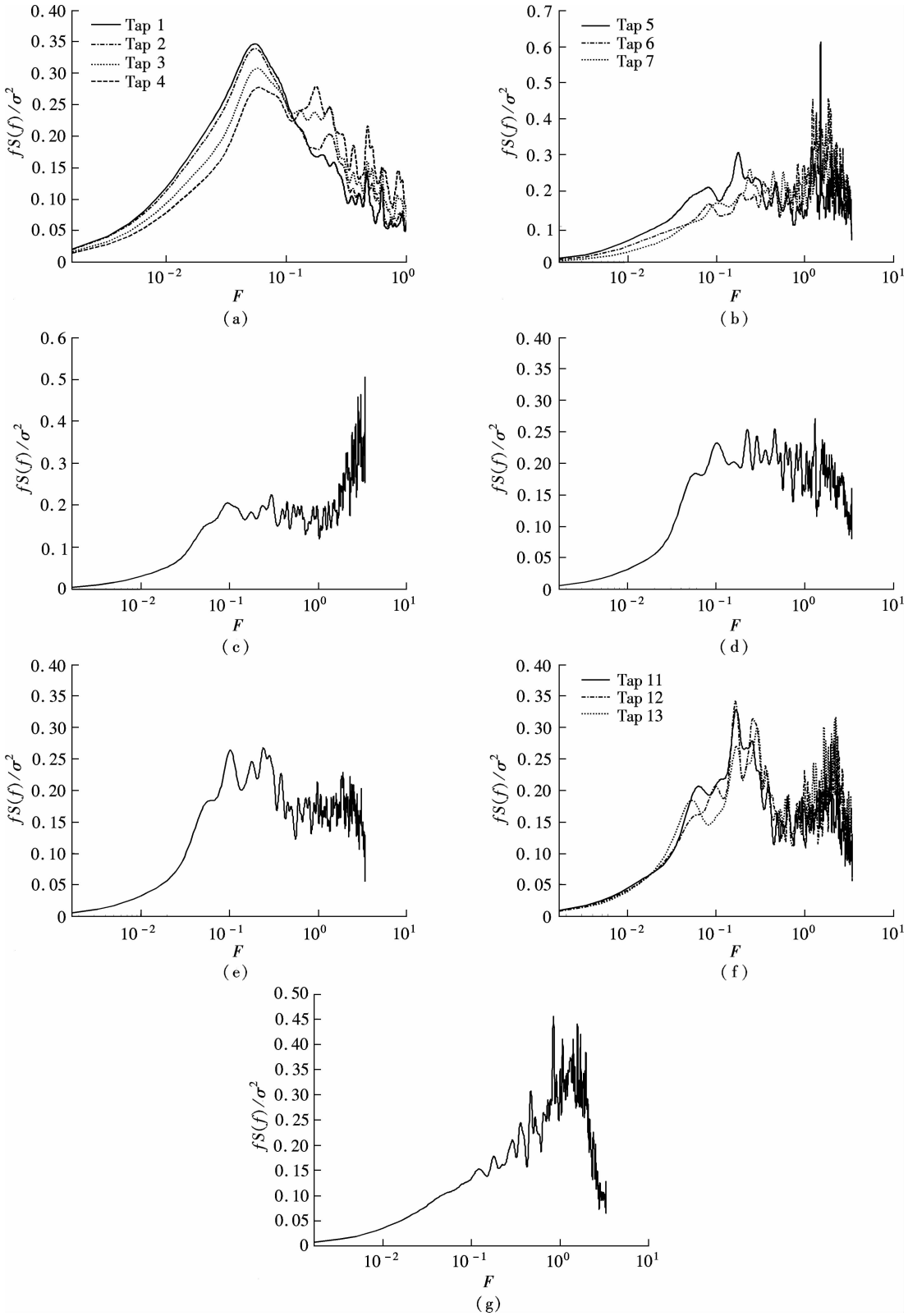

Fig. 5 Wind pressure spectra of taps along the leading edge (a) Tap 1to tap 4; (b) Tap 5 to tap 7; (c) Tap 8; (d) Tap 9; (e) Tap 10; (f) Tap 11 to tap 13; (g) Tap 14

and high-frequency ranges increase as tap locations move downstream due to the additional influence of separation of the shear layer. The mean suction and rms values for the taps also increase. From the microcosmic aspect of fluid, shearing processes always exist between fluid layers due to the viscosity of the fluid. The most essential property of shearing is fluid particle spinning. The instantaneous rotational axes of fluid particles form the vortex line, and then form the vortex tube that is capable of creating induced velocity for any point. Then, the roll-up of the shear layer emerges. After flow separation, small-scale turbulence is primarily responsible for the roll-up of the separated shear

layer, while large-scale turbulence allows the vortices to attain maturity before being shed downstream[12]. As shown in Fig. 5(b), the high-frequency content in the wind pressure spectra implies the existence of small-scale turbulence. The vortices, produced by the roll-up of the shear layer, become strong and mature before downward convection, leading to the development of high suctions beneath the vortices. Consequently, the mean suction of the taps tends to increase. This is the separation stage (vortex formation).

The level of high-frequency energy for tap 8 is larger than that of the previous stage, as shown in Fig. 5(c). Further downstream, the vortex becomes mature and stable, which is manifested as well-distributed energy in the wind pressure spectrum for tap 9 (see Fig. 5(d)). The variation gradient of the rms value from tap 8 to tap 9 reaches the maximum value. Thus, the mean suction continues to increase, indicating a decrease in the streamwise velocity[1]. This is a premonition of vortex breakdown. Thus, the current stage is characterized by the oscillation of breakdown location.

As the axial velocity decreases, it must then cause an outward radial flow due to continuity. Once the vorticity becomes negative, it is enhanced due to the outward radial flow and, hence, leads to the vortex breakdown. The possible helical mode instability of the breakdown flow may induce large pressure fluctuations on the roof surface. As shown in Fig. 5(e), the rms pressure coefficient of tap 10, whose spectrum exhibits a wide range of fluctuating energy, is now the highest of all the taps.

The spectra of taps 11, 12, and 13 feature two humps, one at the end of the middle-frequency range and the other at the end of the high-frequency range (see Fig. 5(f)). The energy of the middle frequency range is higher compared to the upper stage. In addition, the turbulence scale is large enough to allow the vortices to reach maturity and stability before being shed downstream. These factors result in the peak suctions of taps 11 and 12. As the high-frequency energy grows due to the development of vortex breakdown, small-scale turbulence increases. The small-scale turbulence, together with vortex breakdown, leads to the decrease in mean suction from tap 12. Lots of small-scale and micro-scale vortices that possess large shear deformation and viscous stress are produced by vortex breakdown. Therefore, turbulence energy dissipation accelerates and is followed by a decrease in the rms value from tap 11. This is the stage of energy redistribution at different frequencies after vortex breakdown.

The wind pressure spectrum of tap 14 displays a single large hump in the high-frequency range (see Fig. 5(g)). The pressure fluctuations at the high points of the saddle roof originate from the building induced small-scale turbulence which can be interpreted as the BIT. The integral scale of the BIT is much smaller than that of the approaching natural wind. Consequently, high-frequency pressure fluctuations are induced for tap 14.

In order to compare different effects of the BIT and the incident turbulence on pressure fluctuations, Fig. 6 gives several wind pressure spectra of typical taps (see Fig. 2).

Figs. 6(a) and (b) show that due to the effect of the BIT, a spectral hump occurs in the high-frequency range for taps near the high point of the saddle roof. The high-frequency energy decreases with the increase in distance from the high point, which implies a decreasing influence of the BIT. In contrast, low-frequency energy related to incident turbulence increases. The spectrum for tap 57 at a relatively flat concavity presents only one hump in the low-fre-

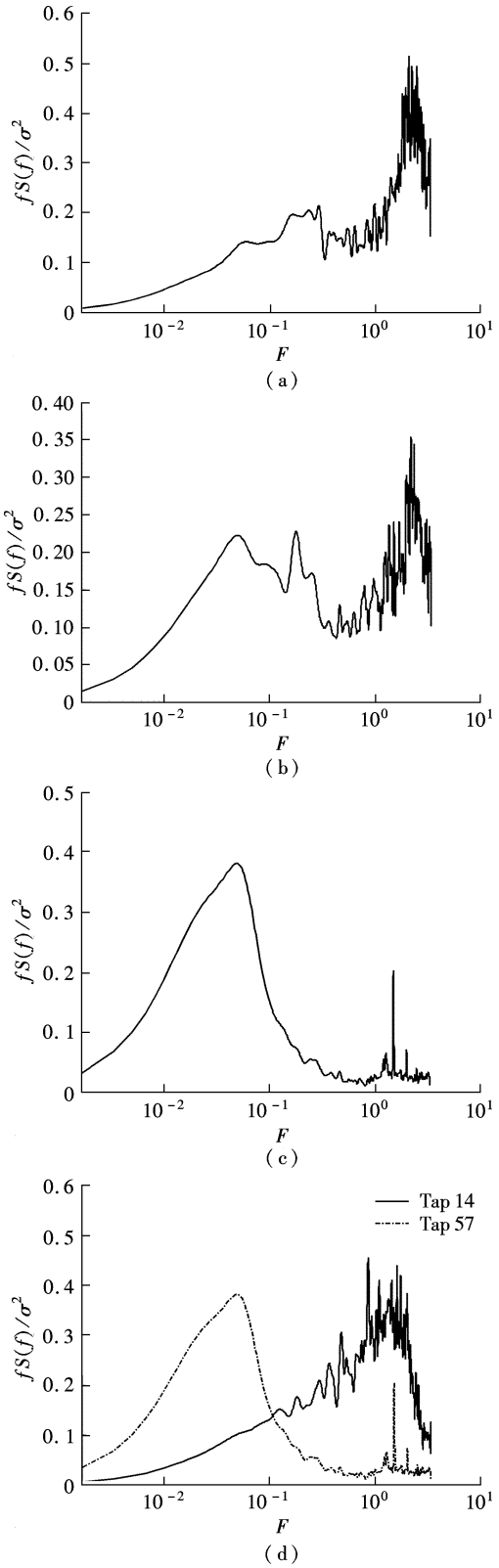

Fig. 6 Wind pressure spectra of typical taps. (a) Tap 26 ($C_{p,rms}$ = 0.218 5); (b) Tap 36 ($C_{p,rms}$ = 0.124 8); (c) Tap 57 ($C_{p,rms}$ = 0.109 6); (d) Tap 14 ($C_{p,rms}$ = 0.241 8) and tap 57 ($C_{p,rms}$ = 0.109 6)

quency range (see Fig. 6(c)), since the pressure fluctuation is the consequence of turbulent content in the incident flow. As a contrast, Fig. 6(d) simultaneously displays the spectra of taps at the central concavity and the high point of the saddle roof. Spectral humps are observed in the low- and high-frequency range, respectively, which reflect distinct influences of the incident flow and the BIT on different frequency bands of pressure fluctuations. Associated with a drop in high-frequency content, the rms value of the above four taps decreases with the increase in distance from the acute high point. Thus, it can be concluded that the BIT is of vital importance to wind pressure fluctuations on the roof surface.

2.3 Non-Gaussian feature of wind pressure

The histograms of the experimental data are used to identify the non-Gaussian feature of wind pressure. Fig. 7 shows the PDF of the selected non-Gaussian samples where the abscissa represents the normalized pressure coefficient. The probability ordinates are drawn in logarithmic scale to clearly show the tail end of the PDF. Furthermore, the normalized Gaussian PDF with zero mean and variance equal to 1 has also been plotted to show the deviation of the measured PDF. It is evident from Fig. 7 that the pressure time series are asymmetric about the mean, exhibiting erratic sharp spikes that are mainly responsible for their non-Gaussian nature.

Although the PDF gives a satisfactory representation of the non-Gaussian nature, it is more useful to have comprehensive indicators for practical design. In this case the skewness and kurtosis, which is 0 and 3 respectively for the Gaussian region, can constitute appropriate tools to identify the non-Gaussian nature of wind pressure, and then classify zones of Gaussian and non-Gaussian pressure fluctuations. Therefore, the skewness and kurtosis, which are higher-order statistical moments, are calculated for all taps. Measured pressure data rarely have absolute values of skewness and kurtosis greater than 0.5 and 3.5, respectively. Therefore, taps with this feature are classified into the non-Gaussian region. Fig. 8 shows the distribution of Gaussian and non-Gaussian regions, among which the shaded part represents the non-Gaussian region. z is assumed to be 10% of the least horizontal dimension or 40% of lower eave height, whichever is less. Of course, z is larger than 4% of the least horizontal dimension or 1 m. It is clear that regions near the leading edges and high points are subject to non-Gaussian fluctuations.

Fig. 9 presents wind pressure spectra of typical taps in Gaussian (tap 34) and non-Gaussian (tap 25, tap 7) regions. The locations of the taps are displayed in Fig. 2. S and k in the parentheses denote the skewness and kurtosis of the sampled taps. Note that the spectrum of the Gaussian region displays a hump in the low-frequency range, while those of the non-Gaussian region show a hump in the high-frequency range. Individually, tap 7 is located in the separated flow region where small-scale turbulence dominates; tap 25 is influenced by the BIT near the high point. Hence, the pressure fluctuations in the Gaussian region are attributed to the fluctuating contents in incident wind, that is, pressures respond to the atmospheric turbulence directly, whereas the non-Gaussian feature of pressure fluctuations originates from the effects of flow separation and the BIT.

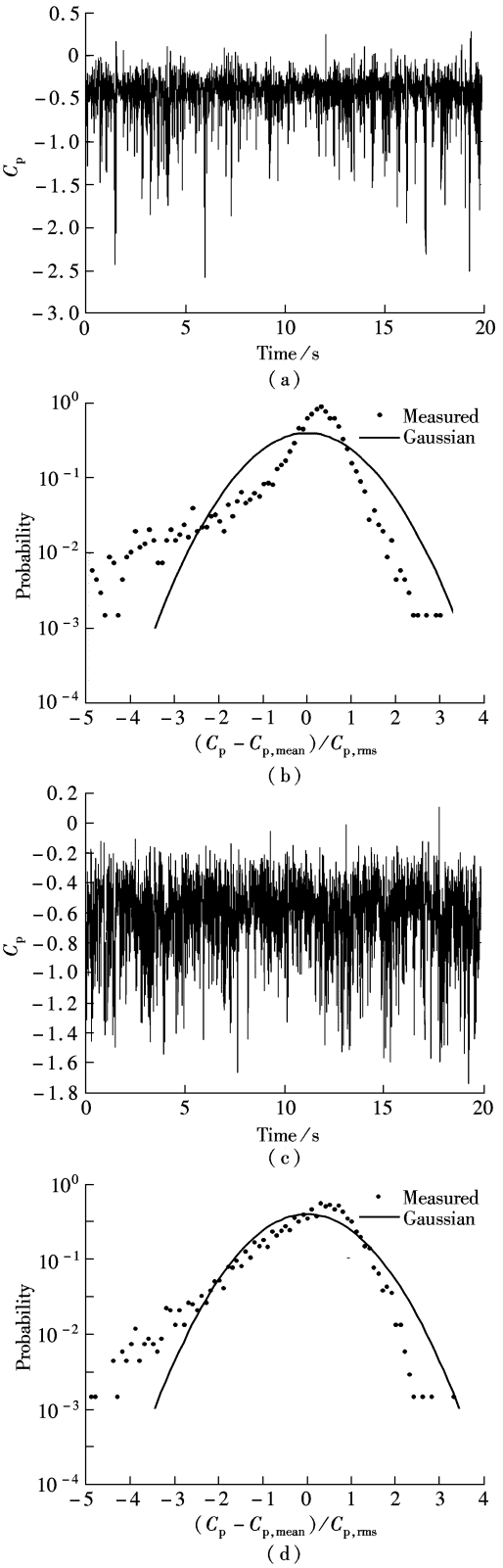

Fig. 7 Measured non-Gaussian pressure coefficient signals and their PDFs. (a) Pressure time history of tap 8; (b) PDF of tap 8; (c) Pressure time history of tap 26; (d) PDF of tap 26

Tab. 3 shows high-order statistical moments of sampled taps (see Fig. 2) in the flow separation region and the BIT influence region. The values of skewness and kurtosis pro-

vide a useful tool to measure the non-Gaussianity of the wind pressure. It appears that the non-Gaussianity of the separation region is more evident than that of the BIT influence area.

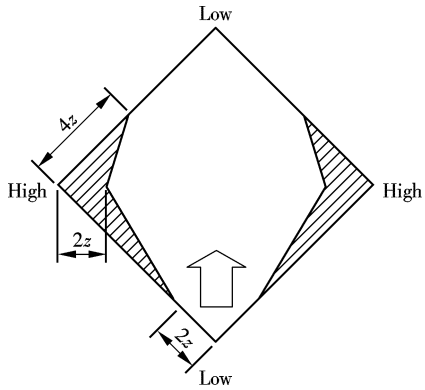

Fig. 8 Gaussian and non-Gaussian zones

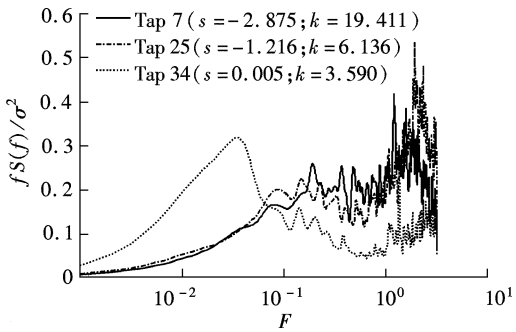

Fig. 9 Sample wind pressure spectra of Gaussian and non-Gaussian regions

Tab. 3 High-order statistical moments of selected samples in the non-Gaussian region

Sample	Skewness	Kurtosis	Region
6	−3.208	20.010	Separation region
7	−2.875	19.410	Separation region
8	−2.628	13.790	Separation region
14	−0.788	4.562	BIT influence area
25	−1.216	6.136	BIT influence area
26	−1.021	4.672	BIT influence area

3 Conclusions

Wind tunnel experiment has been conducted to examine the characteristics of mean and fluctuating pressure on a saddle roof at a wind direction of 0°. By analyzing the experimental data, the mechanism of wind pressure distribution along vulnerable leading edges is discussed. The non-Gaussian feature of the wind pressure is studied. The main conclusions of this work can be summarized as follows:

1) After flow separation, the incident small-scale turbulence is responsible for the increased roll-up of the separated shear layers, while large-scale turbulence allows vortices to reach maturity before being convected downstream. As a result, peak suctions occur in the vicinity of the high points. Nevertheless, the high points are not the location of peak suctions, due to previous vortex breakdown. Large suction fluctuations occur at the high points and in the surrounding regions due to the additional effect of the BIT, which is shown as a hump in the high-frequency range of wind pressure spectra.

2) The high suctions at the central concavity are associated with flow separation at the central region after the flow streams down along the windward curved roof. However, the suction fluctuations at the central concavity, influenced by the incident turbulence that displays itself as low frequency humps in the wind pressure spectra, are not intense due to the flat curvature and less prominent effect of the BIT.

3) The Gaussian and non-Gaussian zones of pressure fluctuations are all found on the roof surface, among which the non-Gaussian zones are located near the leading edges and high points. When the pressure on the roof responds to the atmospheric turbulence directly, it is subject to the Gaussian fluctuation. The non-Gaussian feature of wind pressure originates from the effects of flow separation and the BIT, and the former effect plays an obvious role.

References

[1] Chen Meifa. Characterization of wind pressure fluctuations on a gable roof house[D]. Clemson, SC, USA: Civil Engineering of Clemson University, 2000: 63−76.

[2] Kasperski M, Koss H, Sahlmen J. BEATRICE joint project: wind action on low-rise buildings, Part 1: basic information and first results[J]. *Journal of Wind Engineering and Industrial Aerodynamics*, 1996, **64**(2/3): 101−125.

[3] Suresh Kumar K, Stathopoulos T. Power spectra of wind pressure on low building roofs[J]. *Journal of Wind Engineering and Industrial Aerodynamics*, 1998, **74/75/76**: 665−674.

[4] Stathopoulos T. PDF of wind pressure on low-rise buildings [J]. *Journal of Structural Engineering*, 1980, **106**(5): 973−990.

[5] Kareem A, Cermak J E. Pressure fluctuations on a square building model in boundary layer flows[J]. *Journal of Wind Engineering and Industrial Aerodynamics*, 1984, **16**(1): 17-24.

[6] Suresh Kumar K, Sathopoulos T. Wind loads on low building roofs: a stochastic perspective[J]. *Journal of Structural Engineering*, 2000, **126**(8): 944−956.

[7] Sun Ying, Wu Yue, Shen Shizhao, et al. Non-Gaussian features of fluctuating wind pressures on long span roofs[J]. *China Civil Engineering Journal*, 2007, **40**(4): 1−5. (in Chinese)

[8] Gioffre M, Gusella V. Non-Gaussian wind pressure on prismatic buildings. Ⅰ: stochastic field[J]. *Journal of Structural Engineering*, 2001, **127**(9): 981−989.

[9] Ko Nag Ho, You Ki Pyo, Kim Young-Moon. The effect of non-Gaussian local wind pressures on a side face of a square building[J]. *Journal of Wind Engineering and Industrial Aerodynamics*, 2005, **93**(5): 383−397.

[10] Hou Xinzhen. Wind tunnel experimental research on rigid models of long span roof[D]. Nanjing: School of Civil Engineering of Southeast University, 2009: 38−61. (in Chinese)

[11] Shen Zhenyuan, Nie Zhiliang, Zhao Xuehe. *Principles of communication system*[M]. Xi'an: Xi'an Electronics Science and Technology University Press, 1993: 280−289. (in Chinese)

[12] Li Q S, Melbourne W H. An experimental investigation of the effects of free-stream turbulence on stream wise surface pressures in separated and reattaching flows[J]. *Journal of Wind Engineering and Industrial Aerodynamics*, 1995, **54/55**: 313−323.

菱形马鞍屋盖表面风压特性的风洞试验研究

董 欣 叶继红

(东南大学混凝土及预应力混凝土结构教育部重点实验室,南京 210096)

摘要:通过刚性模型风洞测压试验,研究了风向沿马鞍低点连线时菱形马鞍屋盖表面的风压特性. 首先给出了屋盖表面的平均及脉动风压分布,通过脉动风压谱,从微观角度阐述了迎风前缘附近旋涡从生成、发展直到最后破裂的过程,进而解释了迎风前缘易损区域的平均及脉动风压分布机理. 分析马鞍高点附近的风压谱形状,发现结构对于来流的干扰作用在风压脉动上体现为高频脉动. 此后用测点风压时程的三、四阶矩对风压的非高斯特性进行描述并给出了划分高斯、非高斯区的标准,在此基础上对马鞍屋盖表面进行了分区. 通过研究脉动风压谱,发现风压非高斯特性是由于来流的分离运动及结构对来流的干扰作用引起的,且前者引起的非高斯特性较后者更为显著.

关键词:马鞍屋盖;风压分布机理;风压谱;非高斯特性

中图分类号:TU312